Word Count: 5,268

The influence of OH content on elastic constants of topaz [$Al_2SiO_4(F,OH)_2$]

Kako Aradachi[1+], Morihisa Hamada[2], Kiyoshi Tsuge[3] and Tohru Watanabe[1]*

1: Department of Earth Sciences, University of Toyama, Gofuku 3190, Toyama, 930-8555 Japan

2: Volcanoes and Earth's Interior Research Center, Research Institute for Marine Geodynamics, Japan Agency for Marine-Earth Science and Technology (JAMSTEC), Natsushima-cho 2-15, Yokosuka, 237-0061 Japan

3: Department of Chemistry, University of Toyama, Gofuku 3190, Toyama, 930-8555 Japan

+: Now at Kankyo Chishitsu Co., Kaizuka 1-4-15-203, Kawasaki-ward, Kawasaki, 210-0014 Japan

*: Corresponding author

ABSTRACT

Topaz, $Al_2SiO_4(OH)_xF_{(2-x)}$, might play a significant role in transporting water and fluorine into the Earth's interior at subduction zones. Seismological detection of topaz gives us insights into the transport of water and fluorine, and requires a thorough understanding of its elastic properties. The influence of OH content on elastic constants of topaz has not been fully understood, though experimental and theoretical studies have been done on topaz with various OH contents. We thus determined elastic constants of topaz for 5 natural single-crystal specimens with different OH content (x=0.28~0.72) via the sphere resonance method at an ambient condition. Determined C_{11}, C_{22}, C_{44}, C_{66}, C_{12}, C_{23} and C_{31} increase with OH content while C_{33} and C_{55} decrease. For the change in OH molar content from 0.0 to 1.0, relatively large changes (>3.0%) are seen in C_{33} (8.0(6)%), C_{55} (4.9(6)%) and C_{22} (3.1(7)%). The OH content dependence of elastic constants is qualitatively similar to that of theoretically determined values except for C_{11}. The theoretical value of C_{11} decreases as the OH molar content increases from 0.0 to 1.0 whereas the experimental value of C_{11} slightly increases. Our determined elastic constants are significantly higher (>3%) than theoretically determined values, especially in diagonal components (C_{ii}). The theoretical lower values must be related to the lattice parameters used in the theoretical study, which are systematically larger than measured

lattice parameters. The theoretical approach should be modified to reproduce measured lattice parameters and lead to the agreement of theoretical and experimental elastic constants. Our results provide a clue to a better understanding of elasticity of topaz and a basis for the seismological detection of subducted oceanic sediments.

Key words: topaz, elastic constants, sphere resonance method, OH content dependence

INTRODUCTION

Topaz is an orthosilicate mineral with ideal formula $Al_2SiO_4(OH)_xF_{(2-x)}$. It is usually found as an accessory mineral in fluorine-rich granitic rocks related to the formation of pneumatolithic/hydrothermal deposits (Pichavant and Manning, 1984; Taylor, 1992; Taylor and Fallick, 1997), or in rock formations that experience ultra-high-pressure metamorphism (Zhang et al., 2002; Alberico et al., 2003). High pressure and temperature experiments on Al_2O_3-SiO_2-H_2O ternary system, which represents subducted oceanic sediments, have shown that hydrous aluminosilicate minerals like phase pi ($Al_2Si_2O_7(OH)_3$) and topaz-OH can retain water up to ~8 GPa (Wunder et al., 1993a, b; Schreyer, 1995). Later, high pressure experiments on a synthetic oceanic sediment revealed that topaz-OH is stable at pressures from 8 to 12 GPa and transforms to another

hydrous aluminosilicate mineral phase Egg ($AlSiO_3(OH)$) at pressures beyond 12 GPa, which can carry water to the mantle transition zone (Ono, 1998). The difference in the stability field of topaz-OH reflects the difference in the chemical composition of their starting materials. The hydroxy-rich topaz, thus, might play a significant role in transporting water into the Earth's interior (Mookherjee et al., 2016; Ulian and Valdrè, 2017; Sema and Watanabe, 2017; Tennakoon et al., 2018).

Topaz might also be a major carrier of fluorine into the Earth's interior (Ulian and Valdrè, 2017; Sema and Watanabe, 2017). Halogens, especially fluorine (320 ppm) and chlorine (850 ppm), are relatively abundant in oceanic sediments (Carpenter, 1969; Muramatsu and Wedepohl, 1998). Fluorine ions can substitute for hydroxy groups in many hydrous minerals because of their similar ionic charges and radii (Pyle and Mather, 2009). Seismological detection of topaz gives us insights into the transport of water and fluorine in subduction zones. It requires a thorough understanding of elastic properties of topaz with a wide range of OH content.

Elastic constants of topaz were firstly determined by Voigt (1888) through bending and twisting of single-crystal prisms. Later, Haussühl (1993), Sema and Watanabe (2017) and Tennakoon et al. (2018) determined elastic constants of topaz with various chemical compositions through the resonance method. Though the temperature dependence of

elastic constants was investigated by Sema and Watanabe (2017) and Tennakoon et al. (2018), these measurements have been conducted only at atmospheric pressure. The pressure dependence of elastic constants has been studied through the *first principles* calculation by Mookherjee et al. (2016) and Ulian and Valdrè (2017). Mookherjee et al. (2016) determined the elastic constants of topaz-OH while Ulian and Valdrè (2017) evaluated those of topaz with systematically changed compositions (x=0.0~2.0).

The influence of OH content on elastic constants of topaz has not been fully understood, though both experimental and theoretical studies have been done on elastic constants of topaz with various OH contents (Table 1). Determined elastic constant C_{22} is shown in Figure 1 as a function of OH molar content. Experimental works were conducted at ambient temperatures (~300 K) while theoretical works determined elastic constants at 0 K. It is difficult to see a systematic relationship between the experimentally determined elastic constant and OH molar content. Though the results of Ulian and Valdré (2018) show a systematic change in C_{22} with OH molar content, there is a remarkable discrepancy between two theoretical studies on topaz-OH and there are significant discrepancies between experimental and theoretical values. These discrepancies cannot be explained by the temperature difference between experimental and theoretical works. Lower elastic constants are generally expected at higher temperatures.

Theoretical and experimental studies should be combined to understand the influence of OH content on elasticity of topaz. Theoretical studies are useful for understanding the influence of OH content on elasticity, since the OH content in topaz can be relatively easily controlled. On the other hand, it is difficult to find natural topaz single-crystal samples with wide range of the OH content, which depends on the mineral formation environment (Zhang et al., 2002). However, the experimental determination of elastic constants is still needed to examine theoretical studies. We have thus conducted experimental determination of elastic constants of topaz for 5 different OH contents (x=0.28~0.72) by the sphere resonance method and compared them with results of previous works.

SPECIMENS

Five natural single-crystals of topaz were selected (x = 0.28, 0.38, 0.45, 0.66 and 0.72). Locality, chemical formula, lattice parameters and unit cell volume are listed in Table 2. Chemical compositions were determined by using an EPMA (JOEL, JXA-8500F) at JAMSTEC Yokosuka Headquarters. Topaz has edge-sharing Al-octahedral units and corner-sharing Si-tetrahedral units (Figure S1). The orthorhombic symmetry with *Pbnm* space group was confirmed and lattice parameters were determined by using a single

crystal X-ray diffractometer (Rigaku, VariMax RAPID-DW). Lattice parameters *a* and *b* increase with increasing OH content, while *c* decreases. The unit cell volume increases with OH content.

Each crystal was shaped into a sphere (Figure 2) by the two-pipe method (Bond, 1954). The average and standard deviation of diameter for 30 measurements are shown in Table 2. The ratio of the standard deviation to the average was smaller than 0.04% for all specimens. The density was calculated from the mass and volume of spheres. It decreases with OH content, reflecting the increase in unit cell volume.

Sample FKO is the sphere sample used in Sema and Watanabe (2017). Measurements were remade on this sample and the diameter was corrected to be 6.487(3) mm by using a calibrated micrometer. The OH molar content, *x* was redetermined to be 0.45.

SPHERE RESONANCE METHOD

The sphere resonance method (e.g., Soga and Anderson, 1967) was employed to determine elastic constants. The measurement system is schematically shown in Figure S2. A sphere specimen was held between two ultrasonic transducers (OLYMPUS, V156RM). A function synthesizer (NF Corporation, WF1944B) applied a sinusoidal signal (Vpp = 10.0 V) to the driving transducer and the excited vibration in the specimen

was picked up by the receiving transducer. The lower transducer was placed on a balance to control the specimen-holding force. Measurements were conducted at an ambient temperature (22ºC). The transducers, specimen and balance were placed in a container to reduce the temperature change. The amplitude of the excited vibration was measured by a lock-in-amplifier (Stanford Research Systems, SR884). The frequency range of the sinusoidal signal is shown in Table S1. The frequency was changed by 20 Hz.

Elastic constants were determined to minimize the difference between measured and calculated resonance frequencies, which was characterized by the root mean square relative error given by

$$D = \sqrt{\frac{1}{n}\sum_i \left(\frac{f_i^{meas} - f_i^{cal}}{f_i^{cal}} \right)^2} ,$$

where f_i^{meas} and f_i^{cal} are measured and calculated resonance frequencies, respectively. The *xyz* algorithm (Vissher et al., 1991) was applied to calculate resonance frequencies for a given set of elastic constants. Uncertainties in elastic constants are determined by the least-square method as described in Sema and Watanabe (2017).

ELASTIC CONSTANTS OF TOPAZ

A typical resonance spectrum is shown in Figure S3. It should be noted that the vibration of a specimen is not a free vibration. The specimen-holding force *F* slightly

148 deforms the specimen to change the resonant frequencies from those of free vibration. In
149 addition, the frequency of a maximum amplitude of excited vibration is different from the
150 resonant frequency of the deformed specimen with normalized difference of order $1/(2Q^2)$,
151 where Q is the quality factor of the resonance (e.g., Migliori and Sarrao, 1997). The
152 dissipation of acoustic energy is characterized by $1/Q$. In our measurements, Q is
153 evaluated by the ratio of the frequency of a maximum to the full width at half maximum
154 of the square of amplitude. It is $(1\sim5)\times10^4$ for each specimen and comparable to the values
155 reported by Tennakoon et al. (2018). Thus, the difference between the frequency of a
156 maximum amplitude and the resonant frequency of the deformed specimen is negligible.
157 The frequency of a maximum amplitude can be treated as a resonant frequency of the
158 deformed specimen. Resonance frequencies were measured for 5 different specimen-
159 holding forces (2.0-10.0 gf), and the resonance frequency of free vibration was estimated
160 by extrapolating measured frequencies to F=0 as Sema and Watanabe (2017). Estimated
161 resonance frequencies of free vibration are summarized in Table S3. Elastic constants
162 were determined by using 42 resonance frequencies. Tennakoon et al. (2018) noted that
163 the elastic constants are determined stably if the number of resonance modes considered
164 is more than 35.

165 Elastic constants of five topaz specimens are shown in Figure 3 as a function of OH

166 molar content and listed in Table S4. The difference between measured and calculated
167 resonance frequencies were smaller than 0.2% for all vibration modes (Table S3). Our
168 determined C_{11}, C_{22}, C_{44}, C_{66}, C_{12}, C_{23} and C_{31} increase with OH content, while C_{33} and
169 C_{55} decrease. The elastic constants of Sample FKO (x=0.45) differ from those in Sema
170 and Watanabe (2017) by 0.4% at most. A linear equation $y = a_1+a_2x$ was fitted to the
171 relation between the elastic constant (y) and OH content (x), and estimated a_1 and a_2 are
172 shown in Table S5. The ratio a_2/a_1 is the relative change in an elastic constant for the
173 increase in OH molar content from 0.0 to 1.0. Relatively large changes (>3.0%) are seen
174 in C_{33} (8.0(6)%), C_{55} (4.9(6)%) and C_{22} (3.1(7)%).

175 Elastic constants reported in previous studies are also shown in Figure 3 for
176 comparison. Haussül (1993) and Tennakoon et al. (2018) determined elastic constants of
177 topaz single-crystals by the resonance method for x=0 and 0.58, respectively. Though
178 there are some deviations, experimentally determined elastic constants show consistent
179 changes: C_{11}, C_{22}, C_{44}, C_{66}, C_{12}, C_{23} and C_{31} increase, while C_{33} and C_{55} decrease. Ulian
180 and Valdrè (2017) determined elastic constants for a wide range of OH content by *first*
181 *principles* calculation. Though their theoretical values are significantly lower than
182 experimental values, especially in diagonal components, the OH content dependence of
183 theoretical values is similar to that of experimental values, except for C_{11}. A linear

equation was also fitted to the relation between the theoretical elastic constant (y) and OH molar content (x) for $x \leq 1.0$. The slope a_2 for the theoretical values is also listed in Table S5 for comparison. Similar slopes are obtained for theoretical and experimental values of C_{22}, C_{44}, C_{55}, C_{66} and C_{12}. The largest change is seen in C_{33} both in theoretical and experimental values. The magnitude of change in the theoretical value of C_{33} is almost twice as large as that in the experimental value. The theoretical value of C_{11} decreases as the OH molar content increases from 0.0 to 1.0, whereas the experimental value of C_{11} slightly increases.

DISCUSSION

Discrepancy between experimental and theoretical elastic constants

Elastic constants determined by the *first principles* calculation (Ulian and Valdrè, 2017) are significantly lower than experimentally determined elastic constants, though theoretical and experimental values show similar dependence on OH content except for C_{11} (Figure 3). Theoretical values are determined at the athermal condition (T=0 K), as already pointed out in Introduction, while experimental values at ambient temperature (T=295 K). The difference in temperature cannot explain the discrepancies in elastic constants, since elastic constants will be lower at higher temperatures due to

anharmonicity. The theoretical lower elastic constants must be related to the lattice parameters in the *first principles* calculation. Lattice parameters of topaz in previous and our studies are shown in Figure 4 as a function of OH content. The lattice parameters in Ulian and Valdrè (2017) are 1% larger than measured values in a, 0.8% in b and 1% in c. The larger lattice parameters are attributed to the computational approach used in the *first principles* calculation. The hybrid exchange functional (B3LYP), which was used through the density functional theory, generally overestimates unit-cell volumes (Ulian and Valdrè, 2017). The theoretical approach should be modified to reproduce measured lattice parameters. It will lead to the agreement between theoretically and experimentally determined elastic constants.

Different trends of C_{11} are seen between experimental and theoretical values. Our experimental value slightly increases (1 ± 2 GPa/mol) for the change in OH content from 0.28 to 0.72, whereas the theoretical value significantly decreases (-11 GPa/mol) for the change in OH content from 0.0 to 1.0. Previous experimental values also show an increase with OH content. This difference might also be reconciled by decreasing lattice parameters in theoretical studies.

Anisotropy in compressibility

Linear compressibility is calculated from determined elastic constants and compared with results of previous studies. Komatsu et al. (2003) and Gatta et al. (2006) determined isothermal linear compressibility through hydrostatic compression tests. Ulian and Valdrè (2017) calculated isothermal linear compressibility from the lattice parameters at different pressures which were obtained through the *first principles* simulation. Tennakoon et al. (2018) evaluated adiabatic linear compressibility from the elastic constants determined by the resonance method. Compressibility along the i-th axis β_i is related to elastic compliance S_{ij} as

$$\beta_i = S_{i1} + S_{i2} + S_{i3}$$

Adiabatic elastic compliance is calculated from determined elastic stiffness. Determined adiabatic linear compressibility is listed in Table S6 and shown in Figure 5. Adiabatic linear compressibilities which were calculated from the elastic constants determined by Haussühl (1993) are also shown in Figure 5.

The results on linear compressibility are qualitatively consistent with those in previous studies, though there are small discrepancies in magnitude between previous and our studies. The most compressible axis is the *c*-axis, and the least the *b*-axis. The compressibility along the *a*-axis is slightly lower than that along the *c*-axis. The compressibility along the *c*-axis increases with OH content ($(0.22\pm0.06)\times10^{-3}$ $GPa^{-1}mol^{-}$

238 ^{1}) while that along the *b*-axis decreases ((-0.11±0.06)×10^{-3} $GPa^{-1}mol^{-1}$). That along the *a*-
239 axis shows no significant change ((-0.04±0.08)×10^{-3} $GPa^{-1}mol^{-1}$). These trends are
240 broadly consistent with those of the *first principles* calculation (Ulian and Valdrè, 2017).
241 The compressibility ratio β_a/β_b is 1.41~1.45, and the ratio β_c/β_b 1.48~1.60. Both ratios
242 increase with OH content. The approaching of β_c to β_a at lower OH content is also seen
243 in theoretical results. The higher compressibility along the *c*-axis is basically due to the
244 compressible "tetrahedra-free zones" which are perpendicular to the *c*-axis (Gatta et al.,
245 2006). They reported that the SiO_4 tetrahedron is less compressible than the AlO_4F_2
246 octahedron. There are other tetrahedra-free weak zones which are subperpendicular to the
247 *a*-axis (Figure 6). These weak zones contribute to higher compressibility along the *a*-axis.
248 The isothermal compressibility obtained from hydrostatic compression tests is quite
249 close to our adiabatic compressibility. It is due to the low temperature (T<300 K) where
250 the oscillation of atoms around their equilibrium positions is nearly harmonic not to cause
251 significant thermal expansion (e.g., Poirier, 1991).
252
253 **Anisotropy in seismic velocities**
254 Seismic velocities in a topaz single crystal (MC, x=0.28) at an ambient condition are
255 shown in Figure 7. Velocities in various propagation directions are calculated as solutions

of the Christoffel equation (e.g., Mainprice, 2007). Compressional-wave velocity (V_P) shows relatively large directional variation (Figure 7(a)). The anisotropy parameter AV_P is 11.8%, which is comparable to that of enstatite (Chai et al., 1997b). The highest velocity (9.95 km/s) is in the direction between the *a*- and *b*-axes, and the lowest (8.84 km/s) in the *a*-axis direction. Compressional-wave velocity is relatively low (<9.5 km/s) in the *ca*-plane.

In addition to the velocity variation with propagation direction, shear-wave velocity changes with the polarization direction. In a given propagation direction, the highest and lowest velocities are called the fast shear-wave velocity and slow shear-wave velocity, respectively. The fast shear-wave velocity (V_S1) is high in the *bc*-plane and the *a*-axis direction, while low in the direction between the *a*- and *b*-axes and that between the *a*- and *c*-axes (Figure 7(c)). The slow shear-wave velocity (V_S2) is high in the *a*-axis direction, while low in the direction between *a*- and *b*-axes (Figure 7(d)). The polarization anisotropy, which is characterized by AV_S, is remarkable (12~14%) in the direction between the *a*- and *b*- axes (Figure 7(b)).

Topaz single crystals with higher OH content show similar directional variations in seismic velocities. The directions of the highest and lowest velocities (V_P, V_S1, V_S2) and the maximum AV_S show no changes with OH content. The anisotropy parameters, AV_P

and the maximum AV_S are shown in Figure S4 as a function of OH content. AV_P and the maximum AV_S show only slight changes for the increase of OH content from 0.28 to 0.72, reflecting the weak OH dependence of elastic constants. The increase in AV_P and decrease in the maximum AV_S are attributed to the increase in C_{22} and decrease in C_{55}, respectively (Figure 3). Similar anisotropy parameters are reported for the topaz with the OH content of 0.58 (Tennakoon et al., 2018) and calculated for the fluorine end member topaz (Haussühl, 1993). The elastic constants determined by Ulian and Valdrè (2017) give also similar anisotropy parameters except for the OH content of 1.0. The large value of AV_P is attributed to the decrease in C_{11} (Figure 3).

Isotropic Moduli

The bulk (K) and shear (G) moduli that an isotropic polycrystalline aggregate will show can be evaluated from single-crystal elastic constants through the Voigt and Reuss averaging schemes. Voigt (1928) assumed uniform strain throughout the aggregate, while Reuss (1929) uniform stress. The Voigt average gives an upper bound, and the Reuss average yields a lower bound for an isotropic modulus. Calculated isotropic moduli are shown in Figure 8 and Table S7. The Hill average, which is the arithmetic mean of the Voigt and Reuss averages, is also shown. Figure 8 also shows bulk and shear moduli

292 calculated from the previously reported elastic constants (Haussühl, 1993; Ulian and
293 Valdrè, 2017; Tennakoon et al., 2018). The lower theoretically determined elastic
294 constants of Ulian and Valdrè (2017) yield lower isotropic moduli.

295 The bulk and shear moduli slightly decrease with increasing OH content (Figure 8(a),
296 (b)). The OH content dependence of the bulk modulus is dominated by that of C_{33}, which
297 shows the strongest dependence on the OH content among elastic constants related to the
298 bulk modulus (Figure 3). On the other hand, the OH dependence of C_{33} and C_{55} dominates
299 that of the shear modulus.

300 The difference between the Voigt and Reuss averages is less than 2% for all single-
301 crystal samples. The magnitude of the difference between the two averages reflects the
302 degree of anisotropy in elasticity of a single crystal. For strongly anisotropic olivine
303 (AV_P=24.3%; Webb, 1989), the difference is 3.2% and 3.9% for the bulk and shear moduli,
304 respectively. For moderately anisotropic enstatite (AV_P=13.6%; Chai et al., 1997b), the
305 difference is 1.5% and 1.7% for the bulk and shear moduli. There is little difference
306 between the two averages for nearly isotropic pyrope (Chai et al., 1997a).

307 Compressional- and shear-wave velocities calculated from isotropic moduli are
308 shown in Figure 8 as a function of OH content. Seismic velocities calculated from the
309 previously reported elastic constants are also shown for comparison. Owing to the lower

density, the lower isotropic moduli of Ulian and Valdrè (2017) yield slightly higher compressional-wave velocity. The shear-wave velocity is almost the same as those calculated from experimentally determined elastic constants. A linear equation is fitted to the relation between the velocity calculated from the Hill averages and OH content. Based on this study, the compositional dependence of velocities is dV_P/dx_{OH} = 0.041(1) km/s and dV_S/dx_{OH} = 0.03(1) km/s. On the other hand, the compositional dependence of velocities of Ulian and Valdrè (2017) for $0.0 \leq x \leq 1.0$ is dV_P/dx_{OH} = -0.072 (6) km/s and dV_S/dx_{OH} = -0.03(1) km/s. The difference in the compositional dependence of velocity is mostly attributed to that in the compositional dependence of C_{11} and C_{33} between Ulian and Valdrè (2017) and this study (Figure 3).

IMPLICATIONS

Our study has confirmed the discrepancy between experimentally and theoretically determined elastic constants that was described in Introduction. The discrepancy should be a clue to a better understanding of elasticity of topaz. The theoretical lower elastic constants must be related to the lattice parameters, which are systematically larger than measured values. The theoretical approach should be modified to reproduce the measured lattice parameters. It will lead to the agreement between experimentally and theoretically

328 determined elastic constants and the improvement of the *first principles* calculation. This
329 study will boost our understanding of elasticity of minerals.

330 Our study will be a basis for the seismological detection of subducted oceanic crust.
331 Sema and Watanabe (2017) calculated isotropic seismic velocities in topaz (FKO) of
332 x=0.45 at high pressure (10 GPa) and temperature (300~1400 K), and compared them
333 with velocities in olivine and garnet, which are major components of the overlying wedge
334 mantle and the underlying subducted oceanic crust, respectively. The compressional-
335 wave velocity in topaz is distinctly higher (~ 1 km/s) than that in olivine. On the basis of
336 the weak dependence of isotropic seismic velocities on OH content (Fig.12(b)), at least
337 for the OH content of x=0.0~1.0, topaz should show distinctly higher compressional-wave
338 velocity than olivine. There might be a strong velocity contrast between the overlying
339 mantle and the thin sediment-origin layer at the depth around 300 km. A seismological
340 technique such as the receiver function technique (e.g., Kawakatsu and Watada, 2007)
341 should be applied to detect a thin layer of topaz. It will give us insights into the transport
342 of water and fluorine in subduction zones.

343

344 **ACKNOWLEDGMENTS**

345 F. Sema, M. Fukusawa, S. Urakawa and T. Saito are thanked for their help at the early

346 stage of this work. Mainak Mookherjee and two anonymous reviewers are thanked for
347 their careful reading and constructive comments. This study was partly supported by JSPS
348 KAKENHI Grant Number 22540436.

349

350 **REFERENCES CITED**

351 Alberico, A., Ferrando, S., Ivaldi, G., and Ferraris, G. (2003) X-ray single-crystal
352 structure refinement of an OH-rich topaz from Sulu UHP terrane (Eastern China) –
353 Structural foundation of the correlation between cell parameters and fluorine
354 content. European Journal of Mineralogy, 15, 875-881.
355 Bond, W.L. (1954) Making crystal spheres. Review of Scientific Instruments, 25, 401.
356 Carpenter, R. (1969) Factors controlling the marine geochemistry of fluorine. Geochimca
357 et Cosmochimica Acta, 33, 1153-1167.
358 Chai, M., Brown, J.M., and Slutsky, L.J. (1997a) The elastic constants of a pyrope-
359 grossular-almandine garnet to 20 GPa. Geophysical Research Letters, 24, 523-526.
360 Chai M, Brown, J.M., and Slutsky, L.J. (1997b) The elastic constants of an aluminous
361 orthopyroxene to 12.5 GPa. Journal of Geophysical Research, 102, 14779-14786.
362 Gatta, G.D., Nestola, F., and Boffa-Ballaran, T. (2006) Elastic behavior and structural
363 evolution of topaz at high pressure. Physics and Chemistry of Minerals, 33, 235-

242.

Haussühl, S. (1993) Thermoelastic properties of beryl, topaz, diaspora, sanidine and periclase. Zeitschift für Kristallographie, 204, 67-76.

Kawakatsu, H., and Watada, S. (2007) Seismic evidence for deep-water transportation in the mantle. Science, 316, 1468-1471.

Komatsu, K., Kuribayashi, T., and Kudoh, Y. (2003) Effect of temperature and pressure on the crystal structure of topaz, $Al_2SiO_4(OH, F)_2$. Journal of Mineralogical and Petrological Sciences, 98, 167-180.

Mainprice, D. (1990) A FORTRAN program to calculate seismic anisotropy from the lattice preferred orientation of minerals. Computers and Geosciences, 16, 385-393.

Mainprice, D. (2007) Seismic anisotropy of the deep Earth from a mineral and rock physics perspective. In G.D. Price, and L. Stixrude, Ed., Treatise on Geophysics, Volume 2: Mineral Physics, p. 437-492. Elsevier, Netherlands.

Migliori, A., and Sarrao, J. L. (1997) Resonant Ultrasound Spectroscopy, Applications to Physics, Materials Measurements, and Nondestructive Evaluation, 202 p. John Wiley & Sons, USA.

Momma, K., and Izumi, F. (2011) VESTA 3 for three-dimensional visualization of crystal, volumetric and morphology data. Journal of Applied Crystallography, 44, 1271-

1276.

Mookherjee, M., Tsuchiya, J., and Hariharan, A. (2016) Crystal structure, equation of state, and elasticity of hydrous aluminosilicate phase, topaz-OH ($Al_2SiO_4(OH)$) at high temperature. Physics of the Earth and Planetary Interiors, 251, 24-35.

Muramatsu, Y. and Wedepohl, K.H. (1998) The distribution of iodine in the Earth's crust. Chemical Geology, 147, 201-216.

Ohno, I. (1976) Free vibration of a rectangular parallelepiped crystal and its application to determination of elastic constants of orthorhombic crystals. Journal of Physics of the Earth, 24, 255-279.

Ono, S. (1998) Stability limits of hydrous minerals in sediment and mid-ocean ridge basalt compositions: Implications for water transport in subduction zones. Journal of Geophysical Research, 103, 18253-18267.

Pichavant, M., and Manning, D. (1984) Petrogenesis of tourmaline granites and topaz granites: the contribution of experimental data. Physics of the Earth and Planetary Interiors, 35, 31-50.

Poirier, J.P. (1991) Introduction to the Physics of the Earth's Interior, 264 p. Cambridge University Press, U.K.

Pyle, D.M. and Mather, T.A. (2009) Halogens in igneous processes and their fluxes to the

400 atmosphere and oceans from volcanic activity: A review. Chemical Geology, 263,
401 110-121.
402 Reuss, A. (1929) Berechnung der Fliessgrenze von Mischkristallen auf Grund der
403 Plastzitätsbedingung für Einkristalle. Zeitschift für Angewandte Mathematik und
404 Mechanik. 9, 49-58 (in Germany).
405 Schreyer, W. (1995) Ultradeep metamorphic rocks: the retrospective viewpoint. Journal
406 of Geophysical Research, 100, 8353-8366.
407 Sema, F., and Watanabe, T. (2017) Determination of elastic constants of a single-crystal
408 topaz and their temperature dependence via sphere resonance method, Physics of the
409 Earth and Planetary Interiors, 271, 64-71.
410 Soga, N., and Anderson, O.L. (1967) Elastic properties of tektites measured by resonant
411 sphere technique. Journal of Geophysical Research, 72, 1733-1739.
412 Taylor, R.P. (1992) Petrological and geochemical characteristics of the pleasant ridge
413 zinnwaldite-topaz granite, southern New Brunswick, and comparisons with other
414 topaz-bearing felsic rocks. The Canadian Mineralogist, 30, 895-921.
415 Taylor, R.P., and Fallick, A.E. (1997) The evolution of fluorine-rich felsic magmas:
416 source dichotomy, magmatic convergence and the origins of topaz granite. Terra Nova,
417 9, 105-108.

418 Tennakoon, S., Peng, Y., Mookherjee, M., Speziale, S., Manthilake, G., Besara, T.,
419 Andreu, L., and Rivera, F. (2018) Single crystal elasticity of natural topaz at high-
420 temperatures. Scientific Reports, 8:1372, DOI:10.1038/s41598-017-17856-3.
421 Ulian, G., and Valdrè, G. (2017) Effects of fluorine content on the elastic behavior of
422 topaz [$Al_2SiO_4(F,OH)_2$]. American Mineralogist, 102, 347-356.
423 Vissher, W.M., Miglior,i A., Bell, T.M. ,and Reinert, R.A. (1991) On the normal modes
424 of free vibration of inhomogeneous and anisotropic elastic objects. Jouranl of
425 Acoustic Society of America, 90, 2154-2162.
426 Voigt, W. (1888) Bestimmung der Elasticitätsconstanten von Topas und Baryt. Annalen
427 der Physik, 270, 981-1028 (in Germany).
428 Voigt, W. (1928) Lehrbuch der Kristallphysik, 978 p. Teubner-Verlag, Leibzig (in
429 Germany).
430 Wunder, B. Rubie, D.C., Rossll, C.R., Medenbach, O., Seifert, F., and Schreyer, W.
431 (1993a) Synthesis, stability, and properties of $Al_2SiO_4(OH)_2$: A fully hydrated
432 analogue of topaz. American Mineralogist, 78, 285-297.
433 Wunder, B., Medenbach, O., Krause, W., and Schreyer, W. (1993b) Synthesis, properties
434 and stability of $Al_3Si_2O7(OH)_3$ (phase pi), a hydrous high-pressure phase in the
435 system Al_2O_3-SiO_2-H_2O (ASH). European Journal of Mineralogy, 5, 637-649.

436 Zhang, R.Y., Liou, J.G., and Shu, J.F. (2002) Hydroxyl-rich topaz in high-pressure and
437 ultrahigh-pressure kyanite quarzites, with retrograde woodhouseite, from the Sulu
438 terrane, eastern China. American Mineralogist, 87, 445-453.

439

440

441 **List of figure captions**

442 Figure 1

443 Reported elastic constant C_{22} of topaz as a function of OH molar content. Experimental
444 values (Haussühl, 1993; Sema and Watanabe, 2017; Tennakoon et al., 2018) were
445 determined at ambient temperatures (~300 K) while theoretical values (Mookherjee et al.,
446 2016; Ulian and Valdrè, 2017) at 0 K. The zero-pressure elastic constant of Mookerjee et
447 al. (2016) was interpolated from reported values of orthorhombic topaz-OH at -3.5 and
448 1.2 GPa.

449

450 Figure 2

451 Five specimens of topaz single crystal. (a) Original shape. (b) Sphere specimen.

452

453 Figure 3

454 Determined elastic constants of five topaz specimens as a function of OH molar content.
455 Results of previous works are also shown for comparison. Experimental values (Haussühl,
456 1993; Tennakoon et al., 2018) were determined at ambient temperatures (~300 K) while
457 theoretical values (Mookherjee et al., 2016; Ulian and Valdrè, 2017) at 0 K. The zero-
458 pressure elastic constant of Mookerjee et al. (2016) was interpolated from reported values
459 of orthorhombic topaz-OH at -3.5 and 1.2 GPa.

460

461 Figure 4

462 Lattice parameters as a function of OH molar content. This study, Komatsu et al. (2003),
463 Gatta et al. (2006) and Tennakoon et al. (2018) determined lattice parameters by X-ray
464 diffraction method at ambient temperatures while Mookherjee et al. (2016) and Ulian and
465 Valdrè (2017) by the *first principles* calculation at athermal condition (T = 0 K). A linear
466 equation was fitted to the relation between the lattice parameter and OH content in this
467 study and Ulian and Valdrè (2017) for $0 \leq x \leq 1$. For this study, $a = 4.636(2) + 0.036(4)$
468 x_{OH}, $b = 8.758(7) + 0.10(1)\, x_{OH}$, $c = 8.3962(9) - 0.014(2)\, x_{OH}$. For Ulian and Valdrè (2017),
469 $a = 4.701(1) + 0.020(2)\, x_{OH}$, $b = 8.8698(6) + 0.094(1)\, x_{OH}$, $c = 8.504(1) - 0.031(2)\, x_{OH}$.

470

471 Figure 5

Linear compressibility calculated from determined elastic constants as a function of OH molar content. The compressibility reported in previous studies (Komatsu et al., 2003; Gatta et al., 2006; Ulian and Valdrè, 2017; Tennakoon et al., 2018) are also shown. The values of Haussühl (1993) were calculated from the reported elastic constants. The solid, grey and open symbols are for the directions of *a*, *b* and *c*-axis, respectively.

Figure 6

Crystal structure of topaz viewed along the *c*-axis. There is a tetrahedra-free zone subperpendicular to the *a*-axis, which contributes to relatively high compressibility along the *a*-axis. This figure was created with a free software VESTA (Momma and Izumi, 2011) by using structural parameters determined by Ulian and Valdrè (2017).

Figure 7

Compressional-wave velocity (V_P) and shear-wave velocities ($V_S1 > V_S2$) in a topaz single-crystal MC (x=0.28) calculated from determined elastic constants. The magnitude of polarization anisotropy (AV_S) and polarization plane of the fast shear-wave are also shown. Careware software developed by Mainprice (1990) was used for calculation and stereographic projection.

490

491 Figure 8

492 (a) Bulk and (b) shear moduli as a function of OH molar content. Isotropic moduli are
493 calculated from the determined elastic constants through the Voigt, Reuss and Hill
494 averaging schemes. The solid, open and grey symbols are for the Voigt, Reuss and Hill
495 averaging schemes, respectively. The values calculated from previous studies (Haussühl,
496 1993; Ulian and Valdrè, 2017; Tennakoon et al., 2018) are also shown for comparison. (c)
497 Compressional- and (d) shear-wave velocities calculated from isotropic moduli. Symbols
498 are used as in (a) and (b).

Table 1. Previous studies for detemining elatsic constants of topaz

	Reference	Method
Experimental	Haussühl (1993)	Rectangular-resonance method
	Sema and Watanabe (2017)	Sphere-resonance method
	Tennakoon et al. (2018)	Rectangular-resonance method
Theoretical	Mookherjee et al. (2016)	*First principles* calculation
	Ulian and Valdrè (2017)	*First principles* calculation

Pressure (GPa)	Temperature (K)	Chemical formula
0	293	$Al_2SiO_4F_2$
0	291.9	$Al_2SiO_4F_{1.56}(OH)_{0.42}$
0	293~973	$Al_2SiO_4F_{1.42}(OH)_{0.58}$
-4.9~34.1	0	$Al_2SiO_4(OH)_2$
0~55	0	$Al_2SiO_4F_2$
		$Al_2SiO_4F_{1.75}(OH)_{0.25}$
		$Al_2SiO_4F_{1.50}(OH)_{0.50}$
		$Al_2SiO_4F_{1.00}(OH)_{1.00}$
		$Al_2SiO_4F_{0.50}(OH)_{1.50}$
		$Al_2SiO_4(OH)_2$

Table 2. Locality, chemistry and physical properties of specimens

Specimen	MC	MGK
Locality	Maynard's Claim, Thomas Range, Juab county, Utah state, USA	Mogok township, Pyin-Oo-Lwin district, Mandalay region, Myanmar
Chemical formula	$Al_{2.00}SiO_4F_{1.72}(OH)_{0.28}$	$Al_{2.00}SiO_4F_{1.72}(OH)_{0.38}$
Lattice parameters and unit-cell volume		
a (Å)	4.64719(8)	4.64982(8)
b (Å)	8.79034(16)	8.79869(16)
c (Å)	8.39215(15)	8.39070(15)
V (Å^3)	342.823(11)	343.283(11)
Diameter of sphere		
Average (N=30) (mm)	4.422(3)	4.588(3)
Standard deviation (N=30) (mm)	0.002	0.002
Standard deviation/Average (%)	0.04	0.04
Density (g/cm^3)	3.582(8)	3.572(7)

FKO	OP	KTL
Fukuoka, Nakatsugawa city, Gifu prefecture, Japan	Ouro Preto, Minas Gerais state, Brazil	Katlang, Tharparkar district, Sindh province, Pakistan
$Al_{1.97}SiO_4F_{1.55}(OH)_{0.45}$	$Al_{1.97}SiO_4F_{1.34}(OH)_{0.66}$	$Al_{1.97}SiO_4F_{1.34}(OH)_{0.72}$
4.64956(8)	4.66016(8)	4.66228(14)
8.79758(16)	8.82724(16)	8.8346(3)
8.39106(15)	8.38715(15)	8.3863(2)
343.235(11)	345.017(11)	345.427(17)
6.487(3)	2.666(3)	4.078(3)
0.002	0.001	0.001
0.02	0.04	0.03
3.568(5)	3.562(12)	3.536(8)

This is the peer-reviewed, final accepted version for American Mineralogist, published by the Mineralogical Society of America.
The published version is subject to change. Cite as Authors (Year) Title. American Mineralogist, in press.
DOI: https://doi.org/10.2138/am-2022-8159. http://www.minsocam.org/

Figure 1

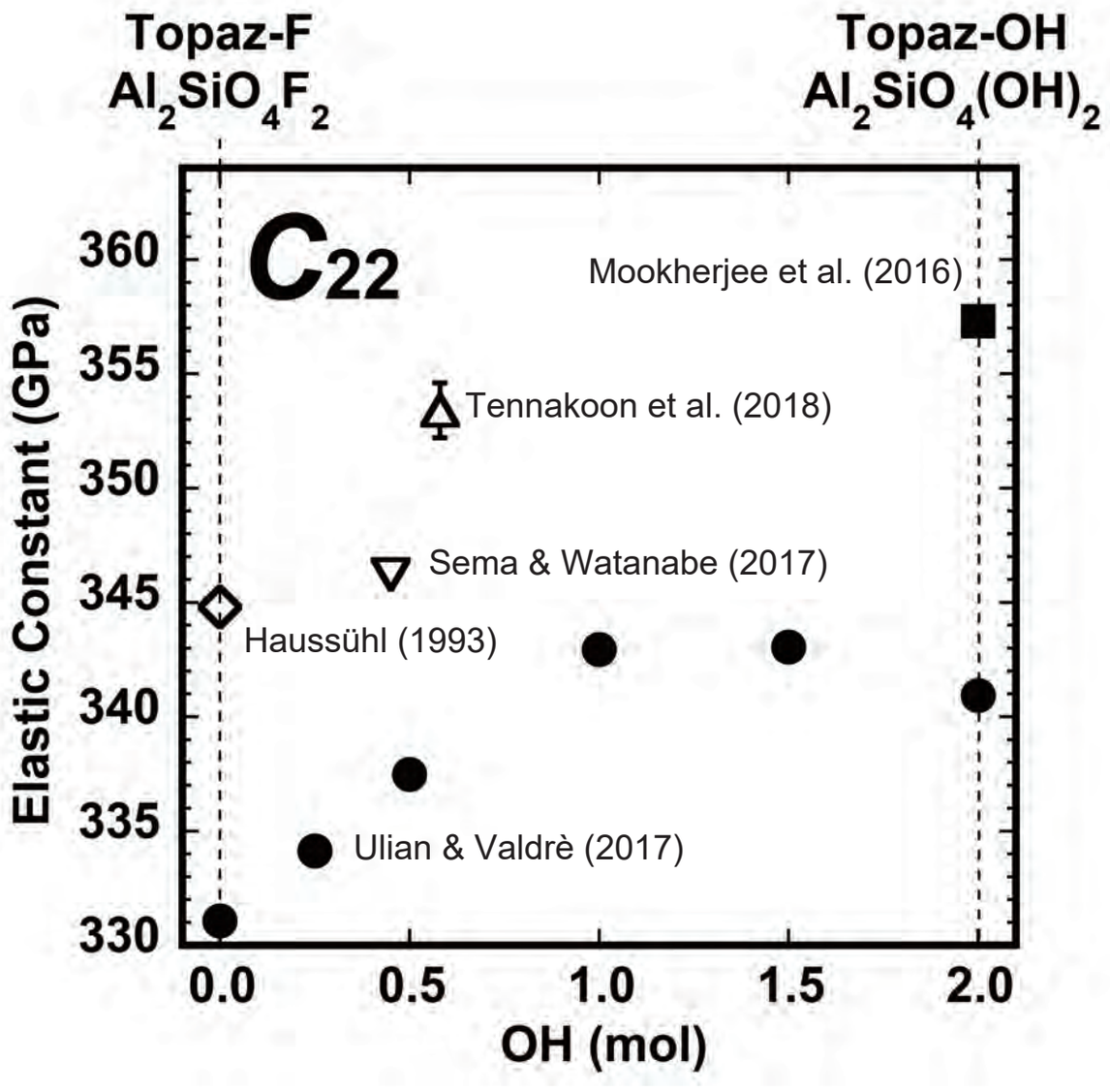

This is the peer-reviewed, final accepted version for American Mineralogist, published by the Mineralogical Society of America.
The published version is subject to change. Cite as Authors (Year) Title. American Mineralogist, in press.
DOI: https://doi.org/10.2138/am-2022-8159. http://www.minsocam.org/

Figure 2

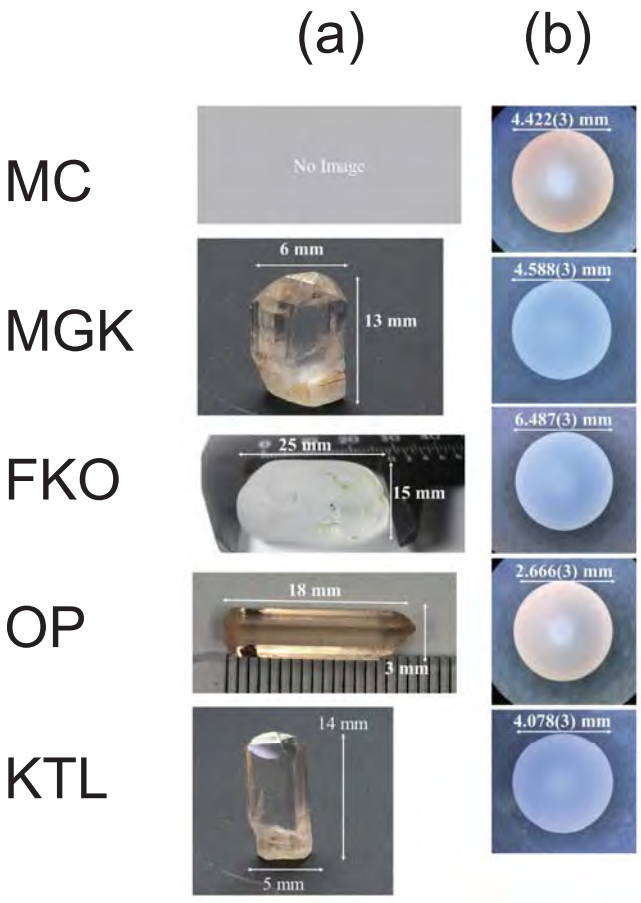

This is the peer-reviewed, final accepted version for American Mineralogist, published by the Mineralogical Society of America.
The published version is subject to change. Cite as Authors (Year) Title. American Mineralogist, in press.
DOI: https://doi.org/10.2138/am-2022-8159. http://www.minsocam.org/

Figure 3

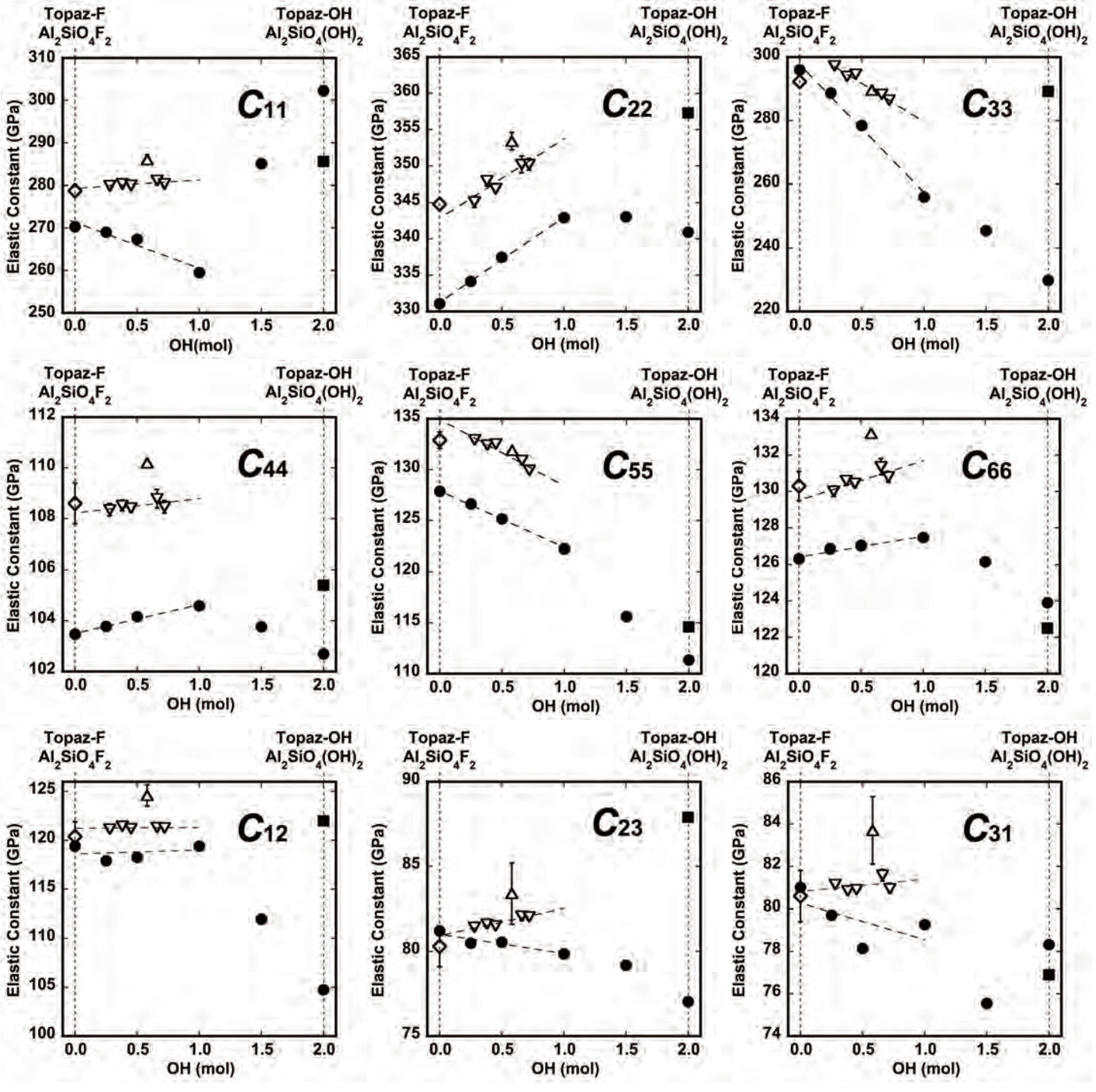

This is the peer-reviewed, final accepted version for American Mineralogist, published by the Mineralogical Society of America.
The published version is subject to change. Cite as Authors (Year) Title. American Mineralogist, in press.
DOI: https://doi.org/10.2138/am-2022-8159. http://www.minsocam.org/

Figure 4

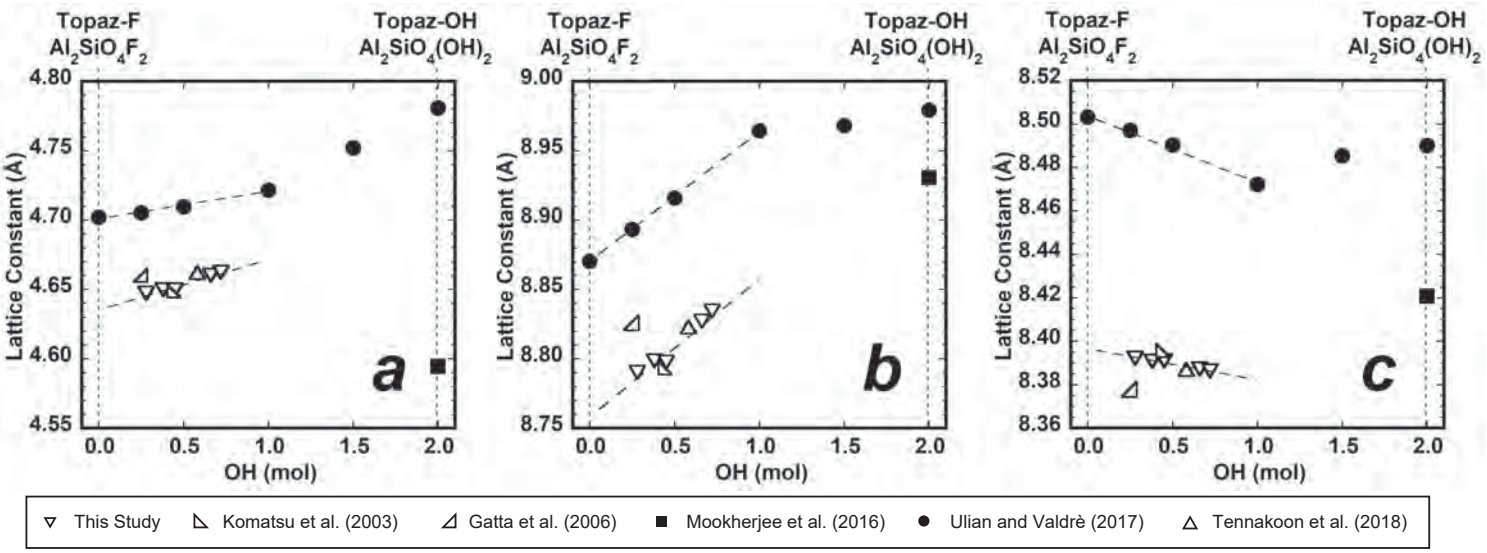

Figure 5

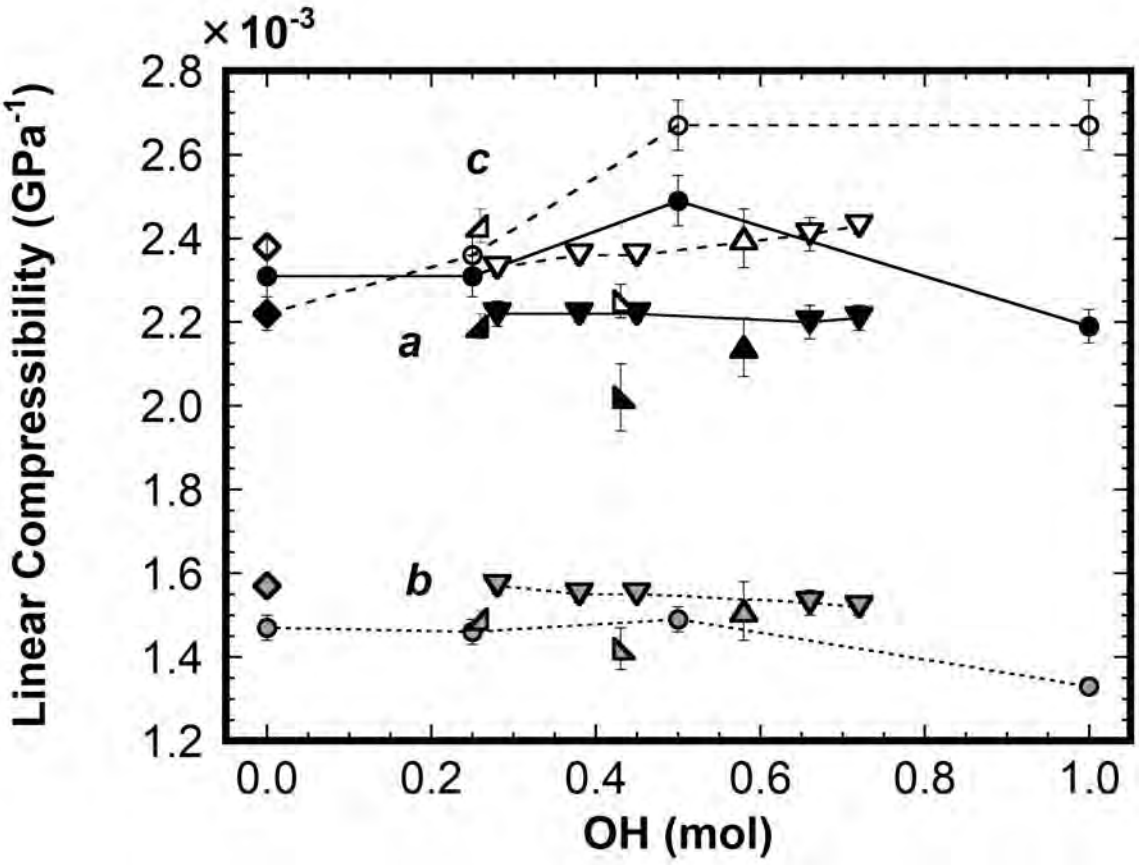

Figure 6

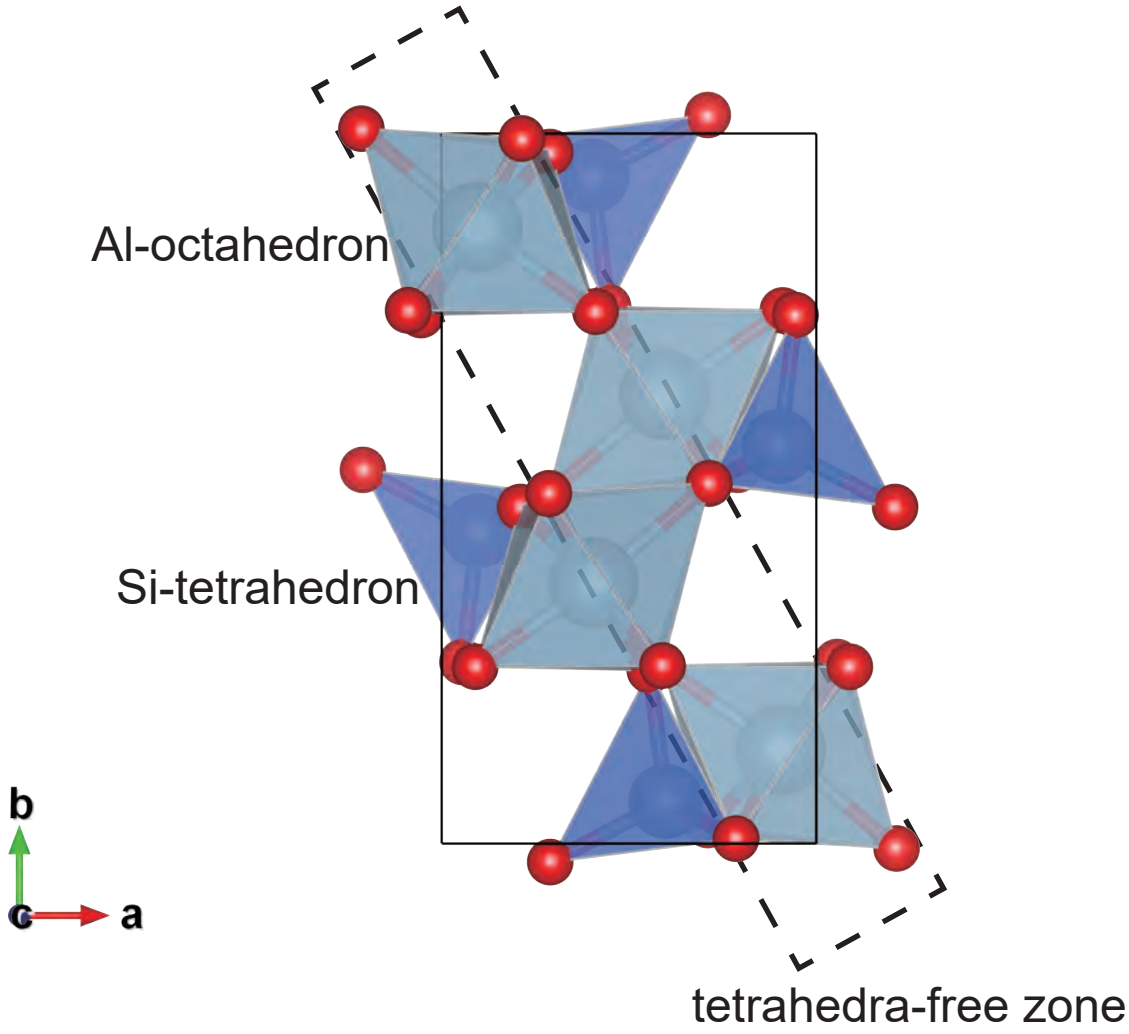

This is the peer-reviewed, final accepted version for American Mineralogist, published by the Mineralogical Society of America.
The published version is subject to change. Cite as Authors (Year) Title. American Mineralogist, in press.
DOI: https://doi.org/10.2138/am-2022-8159. http://www.minsocam.org/

Figure 7

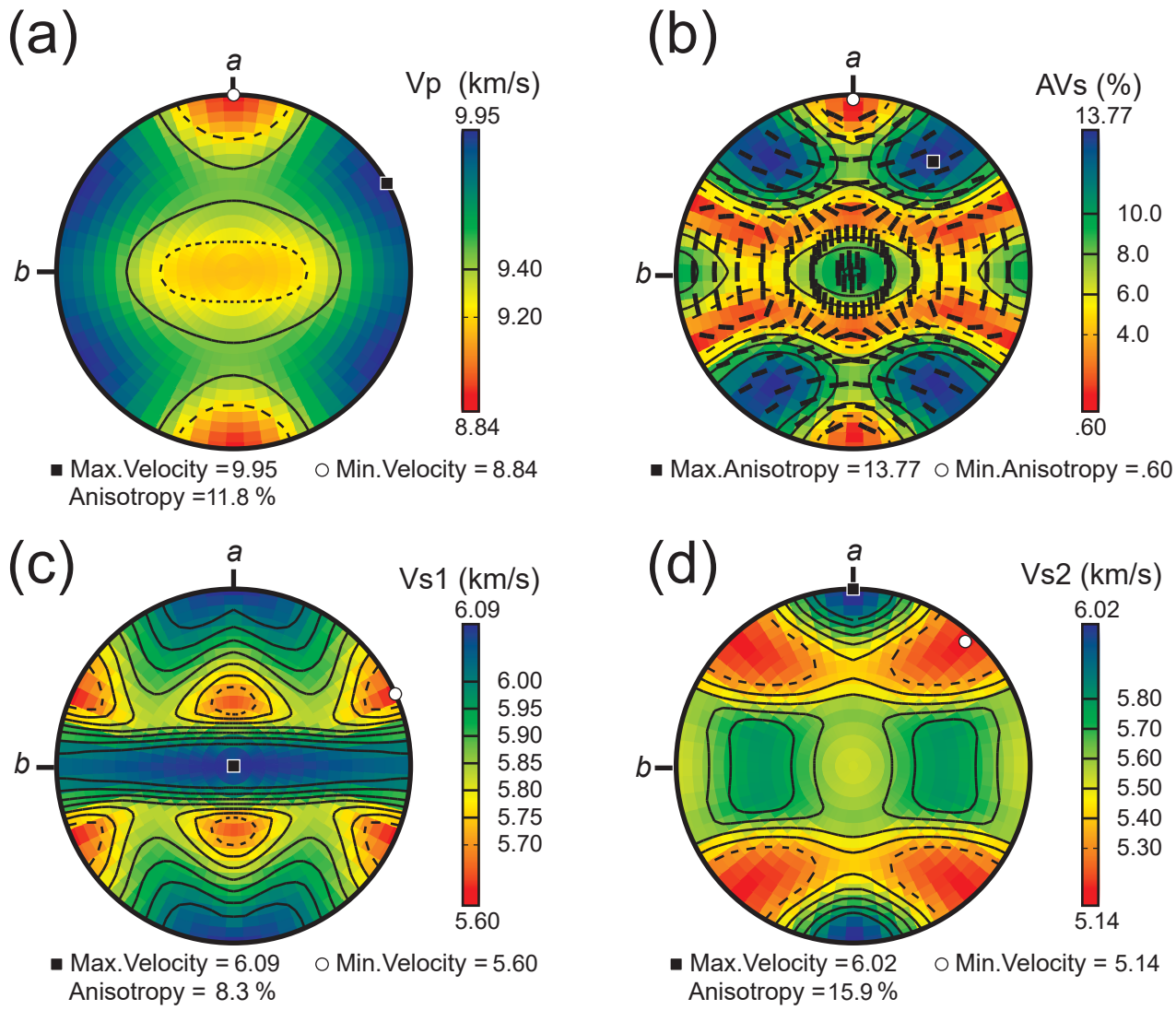

This is the peer-reviewed, final accepted version for American Mineralogist, published by the Mineralogical Society of America.
The published version is subject to change. Cite as Authors (Year) Title. American Mineralogist, in press.
DOI: https://doi.org/10.2138/am-2022-8159. http://www.minsocam.org/

Figure 8